

See discussions, stats, and author profiles for this publication at: <https://www.researchgate.net/publication/345976528>

Reactivity of CuIN₄ Flattened Complexes: Interplay between Coordination Geometry and Ligand Flexibility

Article in Inorganic Chemistry · October 2020

DOI: 10.1021/acs.inorgchem.0c02037

CITATIONS

0

READS

75

5 authors, including:



Leonel C. Llanos
University of Santiago, Chile

9 PUBLICATIONS 57 CITATIONS

[SEE PROFILE](#)



Andrés Vega
Universidad Andrés Bello

160 PUBLICATIONS 1,329 CITATIONS

[SEE PROFILE](#)



Daniel Aravena
University of Santiago, Chile

64 PUBLICATIONS 2,253 CITATIONS

[SEE PROFILE](#)



Luis Lemus
University of Santiago, Chile

24 PUBLICATIONS 110 CITATIONS

[SEE PROFILE](#)

Some of the authors of this publication are also working on these related projects:



Experimental and theoretical study on the oxidation mechanism of dopamine in n-octyl pyridinium based ionic liquids–carbon paste modified electrodes [View project](#)



Graduate PhD Program in Molecular Physical Chemistry [View project](#)

Reactivity of Cu^IN₄ Flattened Complexes: Interplay between Coordination Geometry and Ligand Flexibility

Leonel Llanos, Cristian Vera, Andrés Vega, Daniel Aravena,* and Luis Lemus*



Cite This: *Inorg. Chem.* 2020, 59, 15061–15073



Read Online

ACCESS |

Metrics & More

Article Recommendations

Supporting Information

ABSTRACT: The relation between redox activity and coordination geometry in Cu^IN₄ complexes indicates that more flattened structures tend to be more reactive. Such a preorganization of the ligand confers to the complex geometries closer to a transition state, which has been termed the “entatic” state in metalloproteins, more recently extending this concept for copper complexes. However, many aspects of the redox chemistry of Cu^I complexes cannot be explained only by flattening. For instance, the role of ligand flexibility in this context is an open debate nowadays. To analyze this point, we studied oxidation properties of a series of five monometallic Cu^I Schiff-base complexes, [Cu^I(L_n)]⁺, which span a range of geometries from a distorted square planar ($n = 3$) to a distorted tetrahedron ($n = 6, 7$). This stepped control of the structure around the Cu^I atom allows us to explore the effect of the flattening distortion on both the electronic and redox properties through the series. Experimental studies were complemented by a theoretical analysis based on density functional theory calculations. As expected, oxidation was favored in the flattened structures, spanning a broad potential window of 370 mV for the complete series. This orderly behavior was tested in the reductive dehalogenation reaction of tetrachloroethane (TCE). Kinetic studies show that Cu^I oxidation by TCE is faster as the flattening distortion is higher and the oxidation potentials of the metal are lower. However, the most reactive complex was not the more planar, contradicting the trend expected from oxidation potentials. The origin of this irregularity is related to ligand flexibility and its connection with the atom/electron transfer reaction path, highlighting the need to consider effects beyond flattening distortion to better understand the reactivity of this important class of complexes.

1. INTRODUCTION

For years, copper complexes have been evaluated as a mimic of the active site in metalloenzymes due to the relevance of this metal in biological systems. Copper zinc superoxide dismutase enzyme, CuZnSOD, catalyzes the proton-dependent dismutation of two molecules of superoxide anion to produce dioxygen and hydrogen peroxide, where the copper atom is the redox partner of the superoxide radical, while Zn(II) provides structural stability to the enzyme.¹ In the search for synthetic models of SOD, copper(II) complexes bearing tetracoordinating Schiff-base ligands have been continuously studied.^{2–4} The design of this family of ligands can consider flexible spacers between the Schiff-base moieties to allow the geometrical changes experienced by the copper atom after the electron transfer (ET) in the redox cycle.^{5,4}

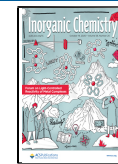
In multicopper oxidases, such as laccase, the active center catalyzes the four-electron reduction of O₂ to water. The tricopper active center in laccase has been a role model for multinuclear copper complexes able to conduct the oxygen reduction reaction (ORR) in electrocatalytic systems, mainly motivated by the development of low-temperature fuel cells.^{5,6} Laccase and related copper-containing enzymes have also been explored for applications of environmental interest, given its

ability to perform dehalogenation reactions in polyhalogenated aromatic substrates, considered as severe contaminants in water effluents and soils.^{7–9} Bio-inspired mono- and polynuclear copper complexes can also react with halogenated substrates, and the reductive dehalogenation has been proposed as the reaction mechanism.^{10–12}

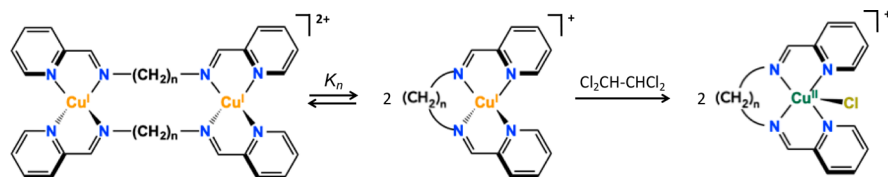
In the chemistry of copper, the redox activity is strongly affected by the coordinative environment around the metal center due to the ET being associated with changes in both the coordination number and geometry around the metal center.^{13,14} About the latter, the most common geometry in Cu^I is tetrahedral, whereas Cu^{II} prefers square-planar, square-pyramidal, or trigonal-bipyramidal geometries.¹⁵ The structural reorganization upon redox activity reduces the ET rates in synthetic compounds, in comparison to copper proteins (10⁴–

Received: July 9, 2020

Published: October 6, 2020



Scheme 1. Representation of the Dissociation Equilibria between the Bimetallic $[\text{Cu}^{\text{I}}(\text{L}_n)]_2^{2+}$ and the Monometallics $[\text{Cu}^{\text{I}}(\text{L}_n)]^+$ Complexes, $n = 3–7$, and Oxidation by Tetrachloroethane



$10^6 \text{ M}^{-1} \text{ s}^{-1}$),^{16,17} where faster ET's are related to the small structural reorganization required for the switching of both oxidation states. In this manner, the protein matrix (ligand) constraints to the metal at the active site and its geometry result in-between that expected for each oxidation state, which is equivalent to a structural conformation closer to the transition state of the reaction. This property in copper and other metalloproteins has been referred as the "entatic state",^{18–20} and it has been also invoked for copper complexes where the ligands impart significant distortions to the geometries leaving the metal in-between the geometries of both oxidation states.²¹

In non-protein coordination complexes, entasis or being "entatic" is often evaluated by the correspondence of the geometries between the reduced and oxidized forms.^{22,23} However, the extension of the entatic state principle from proteins to copper complexes is still under debate.^{24,25} On the one hand, there is the lack of a protein matrix responsible for the geometric distortion and also able to compensate for the energization in the active site. On the other hand, the comparison of the structures for a copper complex in both reduced and oxidized forms does not provide information about the nature of the transition state, which is an inherent part of the entatic state definition.^{26,18,19} Nevertheless, the appeal that the entatic state has as a concept makes it useful to connect geometrical distortions to electronic properties in coordination compounds, and recent reports have spread its applicability to the fields of photophysics^{21,27} and single ion magnets.²⁸

Previously, we have reported on a monometallic complex $[\text{Cu}^{\text{I}}(\text{mphenpr})]^+$, where mphenpr is a tetracoordinating ligand consisting of two phenanthroline moieties tethered by a propyl spacer, which is in equilibrium with the bimetallic helicate $[\text{Cu}^{\text{I}}(\text{mphenpr})]_2^{2+}$.^{29,30} By comparison with the bimetallic helicate where both Cu^{I} atoms are in a tetrahedral geometry, DHA $\sim 87^\circ$ (DHA is dihedral angle formed by two phenanthroline planes), the monomer has a flattened geometry because of the stress produced by the propyl spacer, DHA $\sim 69^\circ$. This flattening induces changes in both the electronic properties and the reactivity of the monometallic complex. Thus, the monometallic complex thermally reacts with CCl_4 by a reductive dehalogenation mechanism, while the bimetallic helicate is unreactive. The reactivity of the monomer is ascribed to the flattened geometry around the Cu^{I} atom, which is closer to the geometry of the oxidized Cu^{II} product, allowing us to lay out a parallel with that enunciated in the entatic state hypothesis.

More recently, we studied a series of homoleptic bimetallic copper(I) complexes, $[\text{Cu}^{\text{I}}(\text{L}_n)]_2^{2+}$, where L_n are bis-Schiff-base ligands with $n = 2–7$ methylene units in the spacer.³¹ These bimetallic complexes dissociate in solution, yielding the monometallic species $[\text{Cu}^{\text{I}}(\text{L}_n)]^+$ (for $n = 3–7$). Both bimetallic and monometallic species have been previously

characterized in solution by spectroscopic techniques,³¹ and we observed that the length of the alkyl spacers provided variable flexibility to modulate the geometry and the electronic properties of the monomers. Consequently, the structures of this series of monometallic complexes transit from the more flattened ($n = 3$) to more tetrahedral ($n = 7, 6$), outlining the spectral features of their metal-to-ligand transition bands, MLCT. In this way, the gradual flattening in the geometry of the monometallic series as the length of the spacer decreases is accompanied by a progressive splitting of the MLCT, in agreement with the strong relationship between the absorption phenomena and geometrical parameters of the N_4-Cu core. Furthermore, the monometallic series $[\text{Cu}^{\text{I}}(\text{L}_n)]^+$ is promptly oxidized by halocarbons such as CCl_4 or more slowly by tetrachloroethane (Scheme 1).

In either the complex derived from mphenpr or those derived from the bis-Schiff-base ligands L_n , the bimetallic species can be considered as precursors of the reactive monometallic complexes. The delivery of the redox active monomers is determined by their dissociation constants, K_n , where aspects such as the presence (or not) of intramolecular π -stacking interactions, even–odd nature, length of the spacers, and solvent are conditions controlling the dissociation equilibria.

In this work, we look deeper into the relationships raised between structure, electronic properties, and reactivity of the monometallic series $[\text{Cu}^{\text{I}}(\text{L}_n)]^+$, $n = 3–7$. This set of complexes, as a whole, can be considered as a stepped tuning of the coordination geometries through the variation of the length of the spacer. Despite the small chemical difference between complexes (the aliphatic linker length), the UV-vis spectrum changes dramatically in this series. This is particularly interesting as more affected bands are related to MLCT transitions, which do not involve the aliphatic chain at all. In this way, we are observing a clean structural effect of the coordination environment due to ligand strain while donor groups remain unmodified along the complete series.

Because spectroscopic differences in this series are important, we expect significant differences in properties sensitive to Cu^{I} flattening such as oxidation potentials or chemical reactivity. In consequence, $[\text{Cu}^{\text{I}}(\text{L}_n)]^+$ ($n = 3–7$) complexes are an ideal test bed to study these properties under strain induced by a flexible ligand, which should resemble a protein environment more than rigid ligands, which are often used for the design of flattened ("energized") Cu^{I} complexes. The relationship between geometry and redox properties is discussed based on electrochemical experiments, and the resultant reactivity is evaluated by reductive dehalogenation of tetrachloroethane. Experimental studies are complemented by a detailed theoretical analysis to establish the link between structure and reactivity. Finally, discrepancies about what it is expected from the relationship between redox–structural properties and reactivity are discussed in terms of the role of

the ligand on the ET's rates, where fresh ideas about the entatic state are considered.

2. RESULTS AND DISCUSSION

2.1. Electronic Structure of $[\text{Cu}^{\text{I}}(\text{L}_n)]^+$. The equilibrium between the bimetallic complexes $[\text{Cu}^{\text{I}}(\text{L}_n)]_2^{2+}$ and their monometallic species $[\text{Cu}^{\text{I}}(\text{L}_n)]^+$ was previously studied in acetonitrile.³¹ In general terms, the equilibrium is shifted to the monometallic complexes as the total concentration of complex decreases. A noticeable characteristic observed from diluted solutions is the different colors of the monomers, ranging from brown-green for $[\text{Cu}^{\text{I}}(\text{L}_3)]^+$ to red-violet for $[\text{Cu}^{\text{I}}(\text{L}_6)]^+$ and $[\text{Cu}^{\text{I}}(\text{L}_7)]^+$.

Aiming to obtain structural information and also to rationalize the trends found in the spectra of this series, theoretical calculations were performed by using density functional theory (TPSSh/Def2-TZVP/PCM),^{32–35} where equilibrium geometries were obtained for each complex (Figure 1). As expected, the length of the spacer affects the

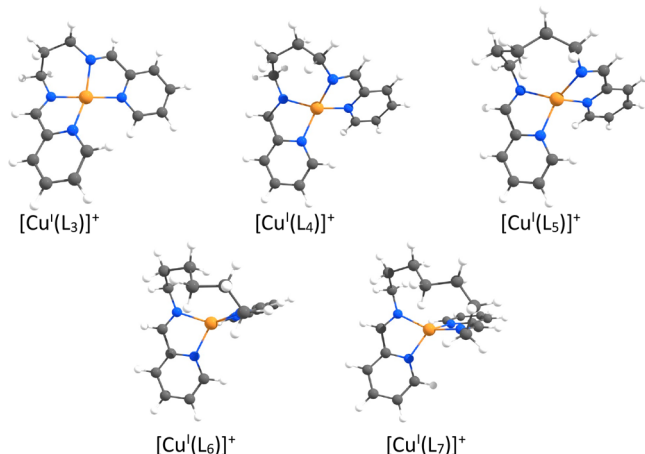


Figure 1. DFT calculated equilibrium geometries for $[\text{Cu}^{\text{I}}(\text{L}_n)]^+$ ($n = 3–7$). Color code: Cu, orange; N, blue; C, gray; H, white.

coordinative environment around the copper atom: The shortening in the spacer tends to flatten the complexes, while the inclusion of methylenes allows more tetrahedral structures. Using the τ_4' parameter as a descriptor of the geometry for tetracoordinated complexes, where $\tau_4' = 1$ for a perfect tetrahedral geometry and $\tau_4' = 0$ for a planar-square geometry,^{36,37} flattening distortions were determined for the set of calculated structures $[\text{Cu}^{\text{I}}(\text{L}_n)]^+$, and τ_4' values of 0.43 ($n = 3$), 0.55 ($n = 4$), 0.59 ($n = 5$), 0.70 ($n = 6$), and 0.66 ($n = 7$) were obtained.

Despite the wide use of the tau index for the structural analysis of coordination compounds, other parameters could better describe the geometrical distortions in tetracoordinated systems lying in-between a perfect tetrahedron (T) and a perfect square-planar geometry (SP) as limit conditions.³⁸ For this purpose, we used continuous shape measurements (CShMs) to quantify the degree of geometric distortion in a systematic way for the set of optimized structures.^{39–41} For each compound, the coordinates of the copper and nitrogen atoms are used as input to calculate its deviation respect to the square-planar (S_{SP}) and tetrahedral (S_{T}) reference geometries. S_{SP} and S_{T} values range from 0 to 33.333, setting the points (0, 33.333) and (33.333, 0) of a plot of S_{T} vs S_{SP} (shape map) as

ideal tetrahedron and square-planar geometries, respectively. These values are used to build a shape map, where the minimal distortion path (black line in Figure 2) serves as a reference to assign a conversion coordinate $\varphi(\text{SP} \rightarrow \text{T})$ between the square-planar and tetrahedral geometries.

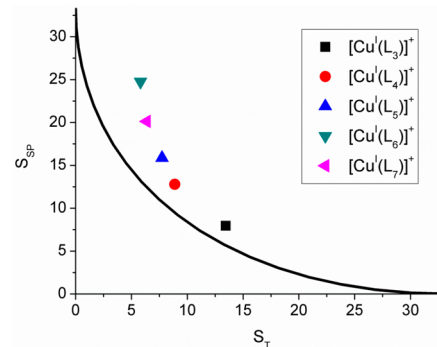


Figure 2. Shape map of the complexes $[\text{Cu}^{\text{I}}(\text{L}_n)]^+$ ($n = 3–7$) and the minimal distortion path between the square-planar and tetrahedral geometry.

The shape map between tetrahedral and square-planar geometries shows that the monometallic complexes follow the trend of the minimal distortion path (Figure 2). Also, the trend is in concordance with the τ_4' values calculated. The difference between points and the minimal distortion path is mainly associated with the bite angle of each coordinating fragment along the series, which is smaller than the angle corresponding to tetrahedral or square-planar geometry. The parameter $\varphi(\text{SP} \rightarrow \text{T})$ shows that an increase in the length of the spacer from three to six methylenes gradually varies the conformation from a square-planar-like geometry to a tetrahedron. The addition of one more methylene unit flattens the structure of the complex $[\text{Cu}^{\text{I}}(\text{L}_7)]^+$, locating it in-between $[\text{Cu}^{\text{I}}(\text{L}_5)]^+$ and $[\text{Cu}^{\text{I}}(\text{L}_6)]^+$ in the shape map. This behavior can be explained considering that the increment of the methylenes in the spacer produces an increase in the separation between imine groups of each coordinating fragment beyond the ideal separation to achieve a D_{2d} -like geometry.

Vertical transition energies between singlet states calculated through TDDFT calculations allowed to simulate the electronic spectra of the complexes. The calculated spectra reproduce the trend observed in the measured spectra (Figure 3), where the short-spaced complexes present two split bands, while the long-spaced compounds show a single band at an intermediate energy. In general, the absorption spectra of tetracoordinated Cu^{I} complexes present one band in the visible region, although splitting in two bands as observed here has been previously reported in the literature.^{42,43} This behavior is associated with distortions from the tetrahedral geometry and the presence of vibronic coupling. Furthermore, the calculated spectrum of $[\text{Cu}^{\text{I}}(\text{L}_7)]^+$ is a good match with the experimental one, locating the maximum of its MLCT band at an intermediate wavelength between $[\text{Cu}^{\text{I}}(\text{L}_5)]^+$ and $[\text{Cu}^{\text{I}}(\text{L}_6)]^+$.

From the analysis of the orbitals involved in the electronic transitions (Table S1), we observe that the lowest energy bands in the flattened complexes (shorter spacers) mainly correspond to a $\text{HOMO} \rightarrow \text{LUMO}$ transition, while the band at higher energy is attributed mainly to the $\text{HOMO}-1 \rightarrow \text{LUMO}+1$ transition. Increasing the tetrahedral character of the complexes mixes these two transitions, increasing the

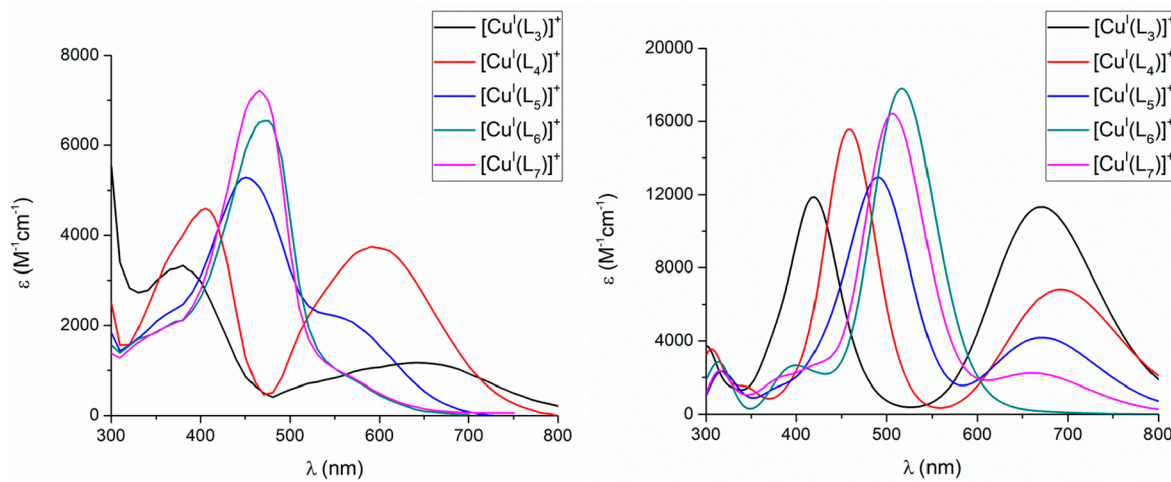


Figure 3. Experimental (left) and calculated (right) UV-vis spectra for $[Cu^I(L_n)]^+$ ($n = 3-7$) in acetonitrile.³¹

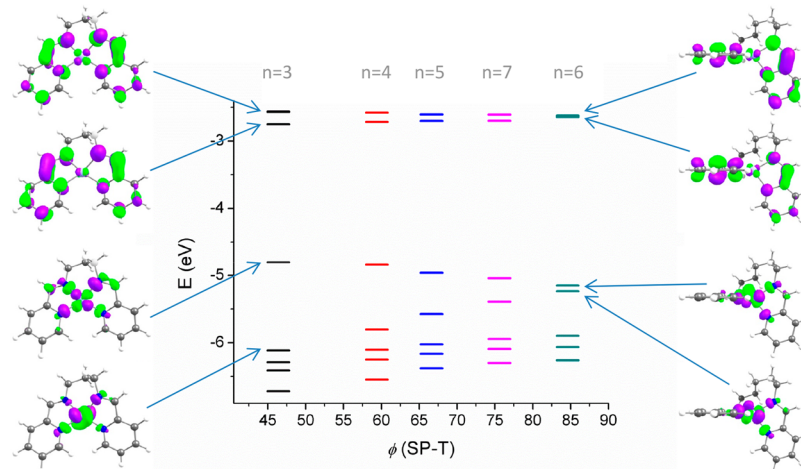


Figure 4. DFT calculated orbital energies for $[Cu^I(L_n)]^+$. The five Cu 3d and two ligand π^* orbitals are presented. The x -axis represents the $\varphi(SP \rightarrow T)$ interconversion coordinate for each complex. Color code: black, $n = 3$; red, $n = 4$; blue, $n = 5$; pink, $n = 7$; cyan, $n = 6$.

energy of the HOMO \rightarrow LUMO transition and decreasing the energy of the HOMO-1 \rightarrow LUMO+1 transition. HOMO to HOMO-4 orbitals correspond to the 3d orbitals from the copper atom, while the LUMO and LUMO+1 are described as a couple of π antibonding orbitals with different phase, delocalized over the imine and pyridine fragments of the ligands. In this way, all the transitions in study are assigned as metal-to-ligand charge transfer (MLCT).

A common coordinate system was chosen for all the complexes to discriminate between d orbitals upon changes of the geometry. The z-axis was oriented so as to contain the midpoints of each pair of nitrogen formed by the pyridine and imine. For instance, the left side in Figure 4 shows the assignment of the d orbitals for $[Cu^I(L_3)]^+$. In this case, the HOMO-1 and HOMO correspond to the d_{yz} and d_{xz} orbitals under this system of reference. A more tetrahedral conformation makes the HOMO-1 and HOMO to be mixes of the d_{yz} and d_{xz} orbitals. On the other hand, the ligand-centered orbitals LUMO and LUMO+1 correspond to π -antibonding orbitals centered on the coordinating fragments of each ligand, both with the same spatial distribution but opposite phase.

Figure 4 shows the molecular orbital diagram for $[Cu^I(L_n)]^+$ ($n = 3-7$), where the position of each complex in the x-axis is the conversion coordinate between the square-planar and

tetrahedral geometries, $\varphi(SP \rightarrow T)$. In this way, flattened Cu^I complexes appear on the left side of the plot, and more tetrahedral geometries are on the right. In the most flattened complex $[Cu^I(L_3)]^+$, there is a separation of 1.31 eV between the d_{xz} (HOMO) and d_{yz} (HOMO-1) orbitals, which gradually becomes smaller as the complexes tend to a tetrahedral geometry, reaching a separation of 0.086 eV for $[Cu^I(L_6)]^+$. On the other hand, the LUMO and LUMO+1 orbitals have a separation of 0.19 eV in the flattened structure, and this separation is reduced to 0.02 eV as the value of $\varphi(SP \rightarrow T)$ increases in $[Cu^I(L_6)]^+$.

The orbital splitting pattern observed in Figure 4 can be explained by applying concepts of molecular symmetry. Approximating the symmetry of the complexes under study to the D_2 point group and preserving the coordinate system established in Figure 4, it is possible to determine the irreducible representation of the relevant molecular orbitals along the distortion path. According to the character table of the D_2 point group, the orbitals d_{xz} (HOMO) and d_{yz} (HOMO-1) transform as the irreducible representations B_2 and B_3 , respectively, while the π -antibonding LUMO and LUMO+1 orbitals of the ligands transform such as B_3 and B_2 . The difference in symmetry between B_2 and B_3 pairs entails electronic transitions at different energies. On the other side, in

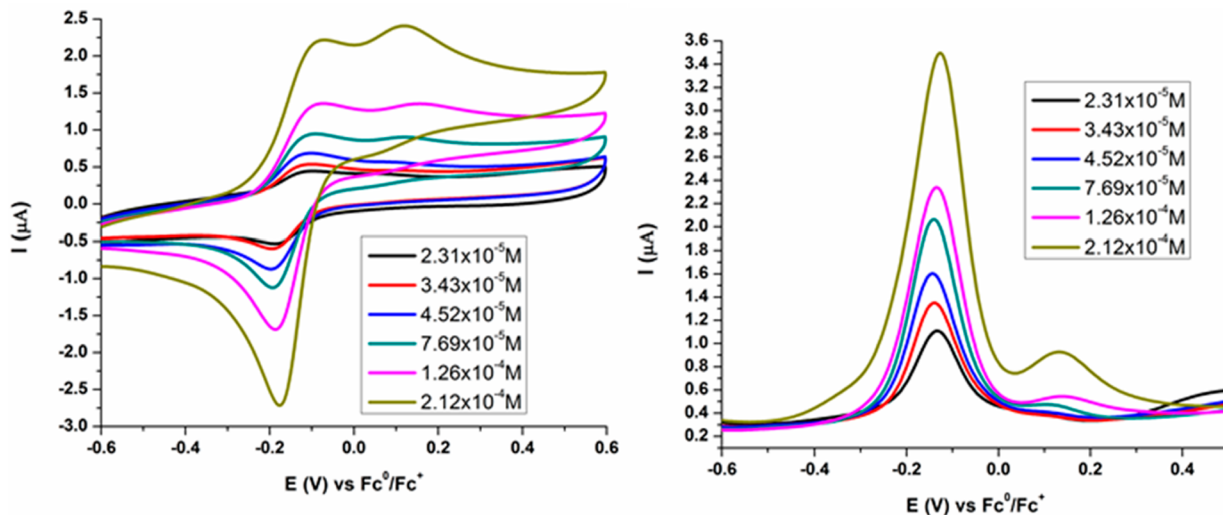


Figure 5. Cyclic (left) and square-wave voltammograms of $[\text{Cu}^{\text{I}}(\text{L}_4)]^+$ at different initial concentrations in TBAP acetonitrile solutions. Scan rate: 100 mV/s.

the ideal D_{2d} symmetry expected for tetrahedral complexes (e.g., orthogonally coordinated bidentate ligands), the pair of d_{xz} (HOMO) and d_{yz} (HOMO-1) orbitals has E symmetry, just like the pair LUMO and LUMO+1, indicating that both pairs of orbitals are degenerate. In other words, orbitals tend to be degenerate as the coordination geometry transits from square planar to tetrahedral. This analysis was previously done by McMillin et al.⁴³ to explain spectral differences in similar Cu^I complexes with polypyridine ligands (Figure S1).

The appearance of two well-defined bands in the experimental spectra of the shorter-spaced complexes, and therefore more flattened, is largely due to the energy separation between HOMO and HOMO-1. From the point of view of orbital overlapping, in a flattened geometry the d_{xz} orbital maximizes its overlapping with electron density from coordinated nitrogens, thus increasing the transition energy. In contrast, flattening of the geometry does not direct the d_{yz} orbital toward the nitrogens, causing an orbital stabilization. By increasing the length of the spacer and reducing the strain in the complexes, the interaction of the orbital d_{xz} with the ligands decreases, causing it to stabilize, while the interaction of the d_{yz} increases going to degeneration.

On the other hand, the splitting of the π -antibonding orbitals LUMO and LUMO+1 allows two transitions of different energy from the HOMO and HOMO-1 orbitals. The transition of the longer wavelength increases its energy by increasing the length of the spacer by the stabilization of HOMO and destabilization of the aforementioned LUMO, while the shorter wavelength transition decreases its energy by destabilizing the HOMO-1 and stabilizing the LUMO-1. This occurs until a tetrahedral geometry is reached, where only one transition occurs due to the degeneration of the orbitals; the calculation reflects this degeneracy as the contribution of the $\text{HOMO-1} \rightarrow \text{LUMO+1}$ transition increases in the $\text{HOMO} \rightarrow \text{LUMO}$ transition, and vice versa.

2.2. Effect of the Structure on the Oxidation Potentials. Considering that the length of the alkyl spacers gradually modifies the coordination geometry around the copper atom in this set of monometallic complexes, this feature of the ligands L_n can also tune the redox potentials. Therefore, we studied the electrochemical processes in the monometallic

series $[\text{Cu}^{\text{I}}(\text{L}_n)]^+$, with $n = 3\text{--}6$, by cyclic voltammetry (CV) and square-wave voltammetry (SWV) experiments (Figure S2). Because of the low solubility of $[\text{Cu}^{\text{I}}(\text{L}_7)]^+$ in acetonitrile solutions of TBAP (0.1 M), this complex was not included in the electrochemical studies.

As the decrease in the initial concentration of the complex increases the [monometallic]/[bimetallic] ratio in the equilibrium,³¹ electrochemical measurements were run at different initial concentrations of each complex to differentiate redox processes belonging to the monometallic or the bimetallic species in equilibrium and also at very diluted solutions where the monometallic complex is predominant.

For $[\text{Cu}^{\text{I}}(\text{L}_4)]^+$, cyclic voltammograms recorded from diluted solutions ($2.3 \times 10^{-5}\text{--}4.5 \times 10^{-5}$ M in Figure 5) show an oxidation peak around -100 mV, with a second process at more positive potentials (shoulder at ~ 100 mV). The raising of the second peak as the concentration of complex increases allows to allocate this process as the oxidation of the bimetallic species $[\text{Cu}^{\text{I}}(\text{L}_4)]_2^{2+}$, while the peak at lower potential can be associated with the oxidation of the monometallic complex. This result is congruent with the more tetrahedral environment around Cu^I in the bimetallic species $[\text{Cu}^{\text{I}}(\text{L}_4)]_2^{2+}$, where more energy must be required for the oxidation of the copper atoms, in comparison to the flattened monometallic species $[\text{Cu}^{\text{I}}(\text{L}_4)]^+$.

In the complexes derived from L_3 , L_5 , and L_6 , anodic peaks corresponding to mono- and bimetallic species are overlapping, and the increase of the concentration from diluted solutions results in the gradual shift of the single and broad peak toward more positive potentials. As observed in the cyclic voltammograms of $[\text{Cu}^{\text{I}}(\text{L}_3)]^+$ (Figure S3), the increase of the concentration produces the sharpening and shifting of the peak at ~ -250 mV to more positive potentials, ~ -200 mV, which reflects the displacement of the equilibrium toward the bimetallic species. This same behavior is observed in the voltammograms of $[\text{Cu}^{\text{I}}(\text{L}_5)]^+$ and $[\text{Cu}^{\text{I}}(\text{L}_6)]^+$ (Figures S4 and S5).

By SWV measurements, oxidation peaks of related mono- and bimetallic complexes can be clearly differentiated in complexes derived from L_3 , L_4 , and L_6 (Figure 5, Figure S3, and Figure S5). For $[\text{Cu}^{\text{I}}(\text{L}_5)]^+$, the overlapping of the

oxidation peaks is observed, and the shift of the single peak at higher potential values occurs when the concentration of complex increases (Figure S4). Table 1 shows the oxidation potentials values obtained by both techniques from diluted solutions.

Table 1. Oxidation Potentials of the Monometallic Complexes Obtained by CV and SWV^a

complex	CV			SWV
	E_{pa} (V)	E_{pc} (V)	$\Delta E/2$ (V)	
$[\text{Cu}^{\text{I}}(\text{L}_3)]^+$	-0.215	-0.328	-0.272	-0.276
$[\text{Cu}^{\text{I}}(\text{L}_4)]^+$	-0.101	-0.194	-0.148	-0.140
$[\text{Cu}^{\text{I}}(\text{L}_5)]^+$	-0.042	-0.112	-0.077	-0.096
$[\text{Cu}^{\text{I}}(\text{L}_6)]^+$	0.157	-0.317	-0.080	-0.008

^aAll potentials are referred to the Fc/Fc⁺ couple, obtained at 0.1 V/s for CV, a frequency of 25 Hz, increasing potential of 0.004 V, and amplitude potential of 0.025 V. Potentials are calculated from the most diluted solutions (inset of Figure 5 and Figures S3–S5).

With regard to the reduction process, a correlation between the potential of the cathodic peak E_{pc} and the length of the spacer is not observed (Table 1). Instead, single peaks appear between -112 and -328 mV, depending on the complex. Single cathodic peaks indicate that the reduction proceeds from a unique Cu^{II} species; this is a cupric monometallic complex. In this way, oxidation of either mono- or bimetallic Cu^I species drives to the formation of monometallic Cu^{II} complexes, where for the case of the bimetallic ones oxidation of the metal must be accompanied by a structural arrangement involving partial dissociation of the ligands.

From the E_{pa} values in Table 1, it is clear that more tetrahedral complexes (longer alkyl spacers) better stabilize the Cu^I state and more energy is required for oxidation. Thereby, it can be established an experimental correlation among length of the spacer, tetrahedral distortion and oxidation potentials through the series. To further explain the trend between measured potentials and geometric distortion, the oxidation potentials were calculated, and a linear relationship is observed between experimental (E_{pa}) and DFT-calculated potentials (Figure 6a). The decomposition of the contributions of energy

to the Born–Haber cycle shows that the ionization potential has the major contribution to the calculated potential, in comparison to solvation energies and thermal contributions. This is consistent with an increase in the HOMO's energy by flattening of the complexes, as shown in Figure 4, allowing the decrease of the ionization potentials and consequently facilitating the oxidation process.

The matching between experimental and theoretical results allows us to assign the shape measure parameter $\phi(\text{SP} \rightarrow \text{T})$ to each complex. From Figure 6b, it can be observed a linear dependence between the oxidation potential and the shape parameter, where the potentials linearly increase as complexes become more tetrahedral. This noticeable correlation indicates that the reductant capability in this series is a linear function of the geometric distortion, thus providing a potential's window of 370 mV by the gradual inclusion of methylenes in the spacer.

3.3. Relation between Structure and Reactivity: Reduction of Tetrachloroethane. The redox reaction between Cu^I and halocarbons proceeds via a reductive dehalogenation mechanism, which involves some Cu^I–halogen interaction in the transition state previous to the electron transfer,^{44,45} and this step could be more difficult as the coordinative environment of the Cu^I atom becomes more tetrahedral.

The stepped flattening of the structures in $[\text{Cu}^{\text{I}}(\text{L}_n)]^+$ allows to systematically evaluate the effect of the geometry on the reactivity in the halogen–carbon cleavage reaction. According to their redox properties, the reactivity should be increasing when their symmetries transit from D_{2d} to D_2 . First, we used CCl₄ as oxidant based on our previous studies.²⁹ However, instantaneous oxidation to Cu^{II} for all the series makes it difficult to establish differences in the reactivity among the complexes. Addition of tetrachloroethane (TCE) to deaerated acetonitrile solutions of the complexes ([TCE] = 100[Cu]) produces changes in their UV–vis spectra, in a period of time ranging from minutes to tens of hours, depending on the complex. Reactions were followed by UV–vis, where a progressive bleaching of the MLCT band besides the rising of bands between 700 and 1100 nm assigned as d–d transitions is congruent with the oxidation of the Cu^I complexes (Figure 7).

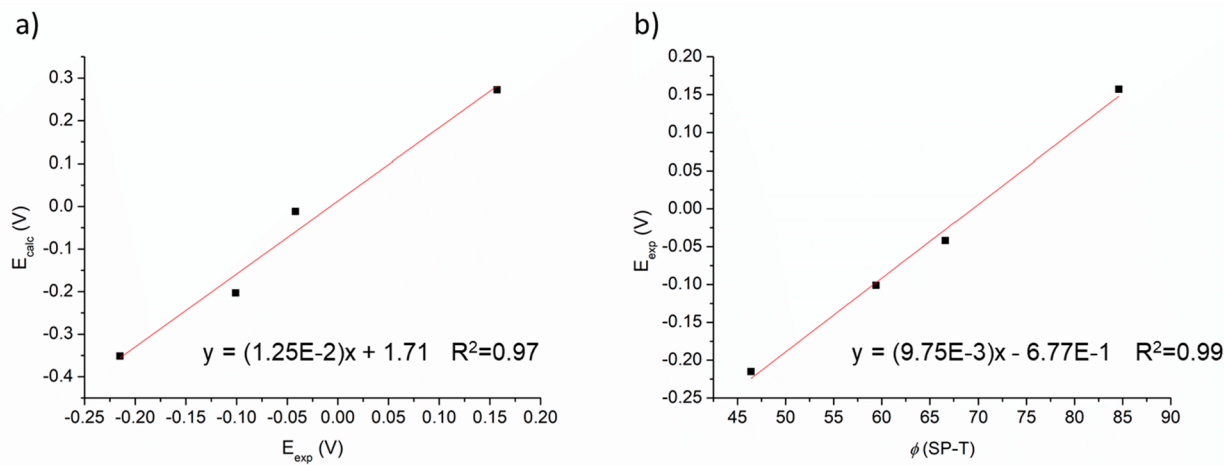


Figure 6. (a) Experimental vs calculated oxidation potentials for $[\text{Cu}(\text{L}_n)]^+$ ($n = 3–6$). (b) Experimental oxidation potential vs shape measure parameter $\phi(\text{SP} \rightarrow \text{T})$ calculated over the optimized structures of each complex. Linear fits (red lines) and its respective linear equations with R^2 values are included in both graphs.

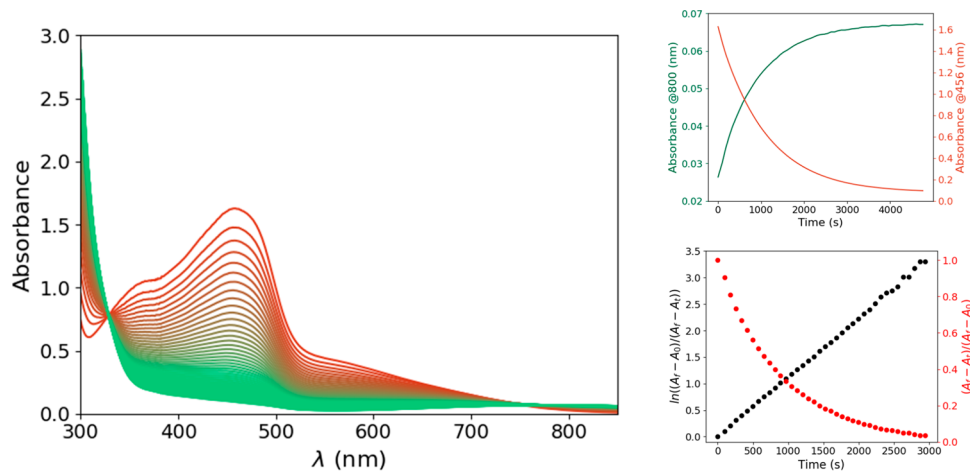


Figure 7. Left: UV-vis spectral variation of $[\text{Cu}^{\text{I}}(\text{L}_3)]^{2+}/[\text{Cu}^{\text{I}}(\text{L}_3)]^+$ ($C_0 = 1.06 \times 10^{-4}$ M) after addition of TCE. The time interval between spectra is 79 s. Right, top: time evolution of absorbance at 800 nm (Cu^{II} formation) and 456 nm (Cu^{I} consumption) after addition of TCE. Right, bottom: time dependence of the 800 nm absorbance linearized for first (black circles) and second (red circles) rate laws.

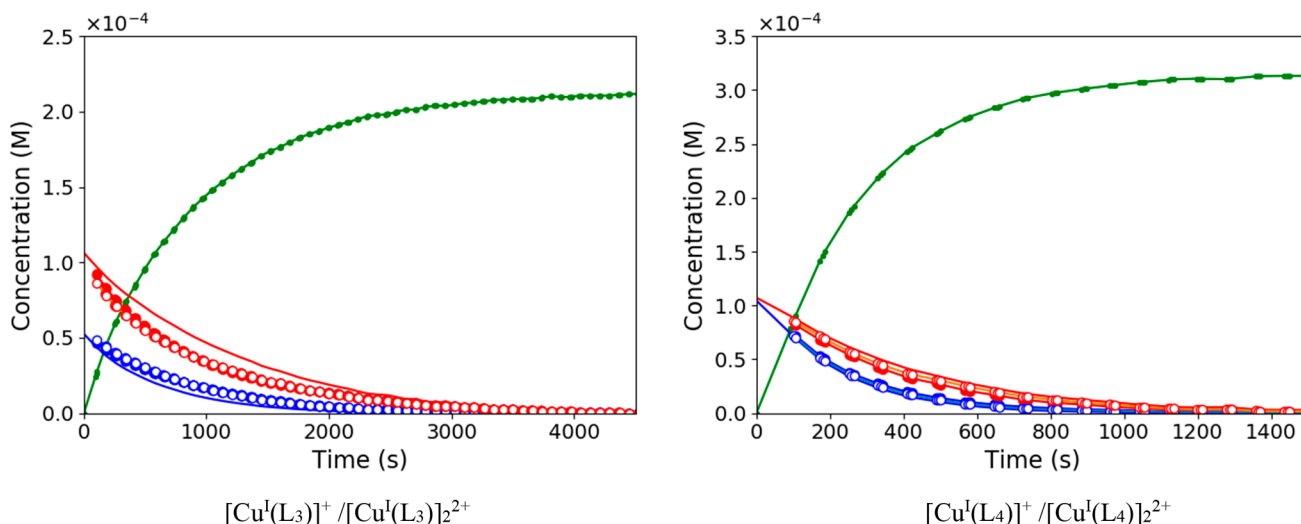


Figure 8. Concentration of oxidized species (green), Cu^{I} monomer (red), and Cu^{II} dimer helicate (blue) as a function of time. Solid lines correspond to concentrations assuming instantaneous equilibration of the folding/unfolding process. Circles correspond to concentrations determined by UV-vis spectroscopy. In the case of $[\text{Cu}^{\text{I}}(\text{L}_3)]^+/[\text{Cu}^{\text{I}}(\text{L}_3)]^{2+}$, filled and empty marks are associated with analysis from the ratio between the spectrum maximum (456 nm) and the absorbances at 554 and 374 nm, respectively. For $[\text{Cu}^{\text{I}}(\text{L}_4)]^+/[\text{Cu}^{\text{I}}(\text{L}_4)]^{2+}$, the reference wavelengths are 367 nm (filled circles) and 590 nm (empty circles). The common peak wavelength is 462 nm.

As discussed in the previous section, oxidation of the monometallic species is shifted at lower potentials with respect to the bimetallic ones, whereby it is possible to suggest that oxidation by TCE occurs in the dissociated monometallic complexes. To support this idea, the bimetallic complex $[\text{Cu}^{\text{I}}(\text{L}_2)]^{2+}$, which does not present measurable dissociation in solution, was maintained in CH_3CN –TCE mixtures for several days, and no oxidation products were observed by UV-vis, while their ^1H NMR spectra in deuterated solvent mixture kept invariable in this time.

Figure 7 shows the reaction of $[\text{Cu}^{\text{I}}(\text{L}_3)]^+$ with TCE for 75 min (initial concentration was $C_0 = 1.06 \times 10^{-4}$ M considering the dimer molecular weight). The kinetic profiles following the bleaching of the MLCT (456 nm) and the growing of the d–d bands (800 nm) indicate that both processes are simultaneously occurring, and no intermediates are detected. The same is observed for the other complexes. Data recorded from the monoexponential growing of the d–d bands can be well

fitted with a pseudo-first-order treatment (Figure 7, right bottom). The lifetime value for $[\text{Cu}^{\text{I}}(\text{L}_3)]^+$ ($\tau_3 = 15.1$ min) is longer than the obtained for $[\text{Cu}^{\text{I}}(\text{L}_4)]^+$ ($\tau_4 = 4.9$ min, $C_0 = 1.58 \times 10^{-4}$ M), while for complexes $[\text{Cu}^{\text{I}}(\text{L}_5)]^+$ and $[\text{Cu}^{\text{I}}(\text{L}_6)]^+$ the lifetimes are between 55–80 min and 933–1250 min, respectively. These intervals are associated with a concentration dependence of the observed lifetime, where higher initial concentrations are related to longer lifetimes (Table S2). This is consistent with a scenario where dissociation equilibrium between Cu^{I} species controls the monomer concentration, affecting the observed reaction constant.

Considering that the complexes have the same N_4 -coordinative core, the trend observed for the lifetime values, $\tau_4 < \tau_3 < \tau_5 \ll \tau_6$, indicates that more flattened complexes derived from short-spaced L_3 and L_4 ligands are oxidized more easily than those derived from flexible ligands L_5 and L_6 . However, the shorter lifetime of $[\text{Cu}^{\text{I}}(\text{L}_4)]^+$ in comparison

Table 2. Dissociation and TCE Oxidation Rate Constants for $[\text{Cu}^{\text{I}}(\text{L}_3)]^+ / [\text{Cu}^{\text{I}}(\text{L}_3)]_2^{2+}$ and $[\text{Cu}^{\text{I}}(\text{L}_4)]^+ / [\text{Cu}^{\text{I}}(\text{L}_4)]_2^{2+}$

	K^{d} (M^{-1})	k_1 (1/s)	k_{-1} (1/M s)	k_2 (1/s)
$[\text{Cu}^{\text{I}}(\text{L}_3)]^+$	2.15×10^{-4}	7.5×10^{-4}	3.4 ± 0.2	$(2.38 \pm 0.04) \times 10^{-3}$
$[\text{Cu}^{\text{I}}(\text{L}_4)]^+$	1.1×10^{-4}	2.6×10^{-3}	25.9 ± 0.3	$(8.9 \pm 0.3) \times 10^{-3}$

^aValues obtained from ref 31.

with $[\text{Cu}^{\text{I}}(\text{L}_3)]^+$ seems to be at odds with the more flattened structure and lower oxidation potential of the latter compound.

To investigate this point further, we tracked the progress of the reaction as a function of the concentration of copper species involved to determine oxidation rate constants for complexes $[\text{Cu}^{\text{I}}(\text{L}_3)]^+$ and $[\text{Cu}^{\text{I}}(\text{L}_4)]^+$, reducing TCE. For this purpose, we take advantage on the strong UV-vis spectral differences between monomeric and dimeric Cu^{I} species. Also, Figure S6 shows the UV-vis spectra of $[\text{Cu}^{\text{II}}(\text{L}_3)]^{2+}$ and $[\text{Cu}^{\text{II}}(\text{L}_4)]^{2+}$, recorded after complete oxidation by TCE.

In the case of $[\text{Cu}^{\text{I}}(\text{L}_3)]_2^{2+}$ and $[\text{Cu}^{\text{I}}(\text{L}_4)]_2^{2+}$, the lowest initial concentrations used in this study fall inside the concentration range used for the determination of dissociation constants,³¹ $C_0 = 1.06 \times 10^{-4}$ M for $[\text{Cu}^{\text{I}}(\text{L}_3)]^+$ and 1.58×10^{-4} M for $[\text{Cu}^{\text{I}}(\text{L}_4)]^+$, expressed as dimer concentration, allowing for interpolation (see Figures S7 and S8). Thus, only these data will be considered for analysis, although general conclusions are valid for all studied concentrations, as shown below. After complete consumption of Cu^{I} species at a long reaction time, the concentration of the oxidized Cu^{II} product will be $2C_0$ since this complex is assumed to be monomeric. Considering this information, molar extinction coefficients for the reaction products can be estimated.

As mentioned, the formation of Cu^{II} products was monitored by the rising of the 800 nm absorbance after addition of TCE (Figure 7), and these curves fit to a monoexponential equation with lifetimes of 15.1 min for $[\text{Cu}^{\text{I}}(\text{L}_3)]^+$ and 4.9 min for $[\text{Cu}^{\text{I}}(\text{L}_4)]^+$. Combining the extinction coefficients of the oxidized species and their time-dependent concentration, the absorption of reaction products can be calculated and subtracted from UV-vis spectra, leaving only the signal corresponding to Cu^{I} compounds.

Knowing the concentration of oxidized species from the analysis of the absorption at 800 nm and the spectrum for the Cu^{I} compounds, the monomer-to-dimer ratio can be calculated from equilibrium data at different initial concentrations. This procedure allows obtaining the concentration of all species during the reaction with TCE (Figure 8). In the case of $[\text{Cu}^{\text{I}}(\text{L}_3)]^+$, we observe that Cu^{I} monomer concentrations (red empty and filled circles) are lower than the ones corresponding to an infinitely fast dissociation equilibrium (solid red line). Consequently, helicate concentrations (blue empty and filled blue circles) are higher than values assuming instantaneous equilibration (blue solid line). Intuitively, this behavior indicates that equilibration of Cu^{I} species is not fully restoring the equilibrium while monomer is consumed by TCE reaction. Interestingly, $[\text{Cu}^{\text{I}}(\text{L}_4)]^+$ shows monomer and dimer concentrations which are closer to the instantaneous equilibrium values, indicating that dissociation equilibrium is faster in this case.

To disentangle dissociation equilibrium and oxidation reactions, we analyze the following kinetic model:

$$\text{D} \rightleftharpoons 2\text{M} \quad K_{\text{eq}} = \frac{k_1}{k_{-1}} = \frac{[\text{M}]^2}{[\text{D}]} \quad (1)$$



where D, M, and O are Cu^{I} helicate, Cu^{I} monomer, and Cu^{II} reaction products, respectively. The rate equations are

$$\frac{d[\text{D}]}{dt} = -k_1[\text{D}] + k_{-1}[\text{M}]^2 \quad (3)$$

$$\frac{d[\text{M}]}{dt} = 2k_1[\text{D}] - 2k_{-1}[\text{M}]^2 - k_2[\text{M}] \quad (4)$$

$$\frac{d[\text{O}]}{dt} = k_2[\text{M}] \quad (5)$$

From the time-dependent concentrations for all species, their time derivatives can be obtained from numerical differentiation. Figure S9 presents the relation between $d[\text{O}]/dt$ and $[\text{M}]$ for $[\text{Cu}^{\text{I}}(\text{L}_3)]^+ / [\text{Cu}^{\text{I}}(\text{L}_3)]_2^{2+}$ and $[\text{Cu}^{\text{I}}(\text{L}_4)]^+ / [\text{Cu}^{\text{I}}(\text{L}_4)]_2^{2+}$, which slope corresponds to k_2 (see Table 2). Observing these plots in detail, a small change in slope can be detected around $[\text{M}] = 0.7 \times 10^{-4}$ M and $[\text{M}] = 3 \times 10^{-5}$ M for $[\text{Cu}^{\text{I}}(\text{L}_3)]^+$ and $[\text{Cu}^{\text{I}}(\text{L}_4)]^+$, respectively. In both cases, the oxidation rate appears to be a bit faster at the beginning of the reaction which could be related to the initial depletion of a slightly more reactive species. Fitting both sections separately, we conclude that the general trend in oxidation rate ($\tau_4 < \tau_3$) is not modified by this process (see Table S3).

Once k_2 is determined, k_1 is calculated either from the helicate or Cu^{I} monomer rate equations.

$$\frac{d[\text{D}]}{dt} = -k_{-1}(K_{\text{eq}}[\text{D}] - [\text{M}]^2) \quad (6)$$

$$\frac{d[\text{M}]}{dt} + \frac{d[\text{O}]}{dt} = 2k_{-1}(K_{\text{eq}}[\text{D}] - [\text{M}]^2) \quad (7)$$

Figure S10 presents the plots for these equations. From the linear regression of both expressions and considering data from two different wavelength ratios, a consistent set of k_{-1} values is obtained (see Table 2).

The kinetic analysis confirms that the reaction of $[\text{Cu}^{\text{I}}(\text{L}_4)]^+$ with TCE is faster than the oxidation of $[\text{Cu}^{\text{I}}(\text{L}_3)]^+$. Explicit consideration of the Cu^{I} equilibration step not changing this trend appears to contradict expectations considering the reductant ability of both complexes (see Table 1 and Figure 6).

At this point, we can infer that factors beyond flattening induced orbital stabilization/destabilization are governing TCE reactivity for these complexes. As structural information can be useful to unveil those factors, crystals of both complexes produced by reaction with TCE were obtained by either slow evaporation of an acetonitrile:TCE mixture or diethyl ether diffusion onto an acetonitrile solution (Figure 9). Expectedly, Cu^{II} centers are now pentacoordinated, where the fifth position is now occupied by a chlorine ion stemming from TCE, confirming the reductive dehalogenation reaction. Selected bond distances and angles are presented in Table 3 (for crystallographic information see Tables S4 and S5).

Contrasting the structure of both complexes, the coordination geometries around the copper atoms are different. In

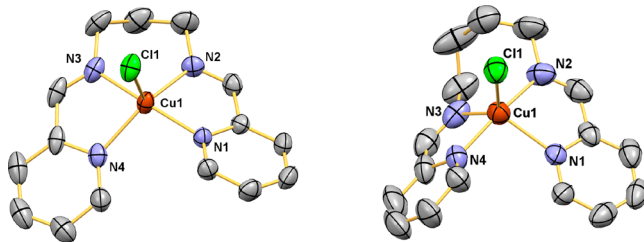


Figure 9. Molecular structures of $[\text{Cu}^{\text{II}}(\text{L}_3)\text{Cl}]^+$ (left) and $[\text{Cu}^{\text{II}}(\text{L}_4)\text{Cl}]^+$ (right). Cu–Cl distances: 2.423 Å (left) and 2.321 Å (right). Ellipsoids at the 50% probability level and hydrogen pictured as arbitrary radii sphere. Perchlorate counteranions were omitted for clarity.

Table 3. Selected Bond Distances (Å) and Angles (deg) Determined for $[\text{Cu}^{\text{II}}(\text{L}_3)\text{Cl}]^+$ and $[\text{Cu}^{\text{II}}(\text{L}_4)\text{Cl}]^+$

$[\text{Cu}^{\text{II}}(\text{L}_3)\text{Cl}]^+$			
Cu1–N3	1.971(3)	Cu1–N4	2.066(3)
Cu1–N1	2.009(3)	Cu1–Cl1	2.4230(9)
Cu1–N2	2.014(3)		
N3–Cu1–N1	168.98(11)	N2–Cu1–N4	146.49(11)
N3–Cu1–N2	91.82(12)	N3–Cu1–Cl1	93.69(9)
N1–Cu1–N2	80.80(11)	N1–Cu1–Cl1	96.63(8)
N3–Cu1–N4	80.91(12)	N2–Cu1–Cl1	111.59(9)
N1–Cu1–N4	100.73(11)	N4–Cu1–Cl1	101.54(8)
$[\text{Cu}^{\text{II}}(\text{L}_4)\text{Cl}]^+$			
Cu1–N4	1.978(5)	Cu1–N1	2.138 (4)
Cu1–N2	1.986(5)	Cu1–Cl1	2.3205 (17)
Cu1–N3	2.054(5)		
N4–Cu1–N2	169.6(2)	N3–Cu1–N1	119.87(18)
N4–Cu1–N3	80.6(2)	N4–Cu1–Cl1	95.05(14)
N2–Cu1–N3	92.7(2)	N2–Cu1–Cl1	95.33(16)
N4–Cu1–N1	96.89(18)	N3–Cu1–Cl1	128.99(15)
N2–Cu1–N1	79.6(2)	N1–Cu1–Cl1	111.12(12)

$[\text{Cu}^{\text{II}}(\text{L}_3)\text{Cl}]^+$, the geometry is closer to a square-pyramidal (SPy) conformation ($S = 1.641$), with the chlorine ion located at the axial position. Deviation with respect to the trigonal bipyramidal (TBPY) is larger in this case ($S = 2.947$). Conversely, $[\text{Cu}^{\text{II}}(\text{L}_4)\text{Cl}]^+$ is closer to a trigonal bipyramidal (TBPY) than to a square pyramid ($S = 1.280$ and 4.832 , respectively), where the chlorine atom is located in the equatorial plane. The geometry index for pentacoordinated complexes, τ_5 (where $\tau_5 = 0$ for SPy and $\tau_5 = 1$ for TBPY),⁴⁶ has a value of 0.38 for $[\text{Cu}^{\text{II}}(\text{L}_3)\text{Cl}]^+$ and 0.68 for $[\text{Cu}^{\text{II}}(\text{L}_4)\text{Cl}]^+$, which is in concordance with results based on shape measures (S values).

A Cu^{II} complex with a structure similar to $[\text{Cu}^{\text{II}}(\text{L}_3)\text{Cl}]^+$ has been reported by Bhattacharyya et al.,⁴⁷ where the Schiff base ligand L has a propyl spacer and also methyl groups on both carbons connecting the pyridine rings with the imine nitrogens. For this complex, a τ_5 value of 0.51 was calculated, which is higher than the observed for $[\text{Cu}^{\text{II}}(\text{L}_3)\text{Cl}]^+$, because of the existence of noncovalent interactions in the packing of the methylated complex.

According to the enunciated in the entatic state principle, where the electron transfer should be faster as the structural variation between both reduced and oxidized forms is minimal, we compared the structures of the complexes in both Cu^{I} and Cu^{II} oxidation states. After overlaying the structures of $[\text{Cu}^{\text{I}}(\text{L}_3)\text{Cl}]^+$ (calculated) with $[\text{Cu}^{\text{II}}(\text{L}_3)\text{Cl}]^{+2}$ (crystal struc-

ture) and comparing with the superimposed structures of the complex derived from L_4 (Figure S11), the expected relationship between minimal distortion and reactivity fails again: the L_3 derived complex has a matching between the Cu^{I} and Cu^{II} structures higher than the L_4 derived complex. This fact was also observed previously for monometallic copper complexes with a high correspondence between the structures of $\text{Cu}^{\text{I}}/\text{Cu}^{\text{II}}$ oxidation states having low electron transfer rates.^{25,48}

These observations open the discussion about the nature of the transition state in Cu^{I} -involved electron transfer reactions, where paradigms such as flattening distortion, redox potentials, and minimal structural distortion do not fully satisfy our experimental results. To shed light on this thought, we calculated the energy profile for the halogen transfer by the inner-sphere electron transfer (ISET) mechanism. ISET has been identified as the energetically favored pathway for similar reactions in the context of copper-catalyzed atom transfer radical polymerization processes.⁴⁹ On the basis of the theoretical results from ref 49, we employed the $\omega\text{B97-XD}$ density functional⁵⁰ and def2-TZVP³³ basis set as this method proved to be accurate for the calculation of activation free energies in similar systems.

A reaction coordinate for reductive dehalogenation of TCE by $[\text{Cu}^{\text{I}}(\text{L}_3)]^+$ and $[\text{Cu}^{\text{I}}(\text{L}_4)]^+$ was calculated performing a relaxed scan varying the C–Cl bond length from its equilibrium value to 2.8 Å, which is enough to observe chlorine transfer. In Figure 10, left, a clear maximum is observed for the unrestricted singlet surface (black) of $[\text{Cu}^{\text{I}}(\text{L}_3)]^+$ at 2.2 Å. The lowest triplet surface is just slightly higher in energy and follows the same trend, while the closed shell singlet grows monotonically in the course of reaction. A similar dependence is observed for $[\text{Cu}^{\text{I}}(\text{L}_4)]^+$ (presented in Figure S12). The activation energy for $[\text{Cu}^{\text{I}}(\text{L}_4)]^+$ is lower than $[\text{Cu}^{\text{I}}(\text{L}_3)]^+$ by 4.5 kcal/mol, in line with the faster kinetics of the former complex.

Comparing the geometries at the energy maximum, we observe that the chlorine atom in $[\text{Cu}^{\text{I}}(\text{L}_3)]^+$ is at the axial position of a square pyramid, while the coordination geometry of the CuN_4 fragment for $[\text{Cu}^{\text{I}}(\text{L}_4)]^+$ is not particularly planar and the chlorine atom can be associated with an equatorial position at a distorted trigonal-bipyramidal conformation. A more quantitative analysis of geometric distortions of the copper coordination environment along the reaction will be presented later.

A quick analysis of the spin density of the unrestricted singlet reveals a different electronic structure before and after chlorine transfer (see Figure S13). Concomitant with the energy maximum, electron transfer occurs and TCE charges negatively by ca. 0.5 electrons. Both fragments now host an unpaired electron. A similar behavior is described in the literature for bromide transfer in a polypyridine– Cu^{I} complex.⁴⁹

Geometry distortion for the CuN_4Cl fragment along the reaction path was quantitatively analyzed by means of continuous shape measurements (see Computational Details for further methodological information). To avoid a bias in distortion measurements by the drastic change in M–L distance associated with the chlorine approach, all metal–ligand distances were normalized. Figure 11, left, shows CShMs for $[\text{Cu}^{\text{I}}(\text{L}_3)]^+$. Before chlorine transfer, structural distortion parameters (S) with respect to the trigonal bipyramidal (solid lines) and square pyramid (dashed lines)

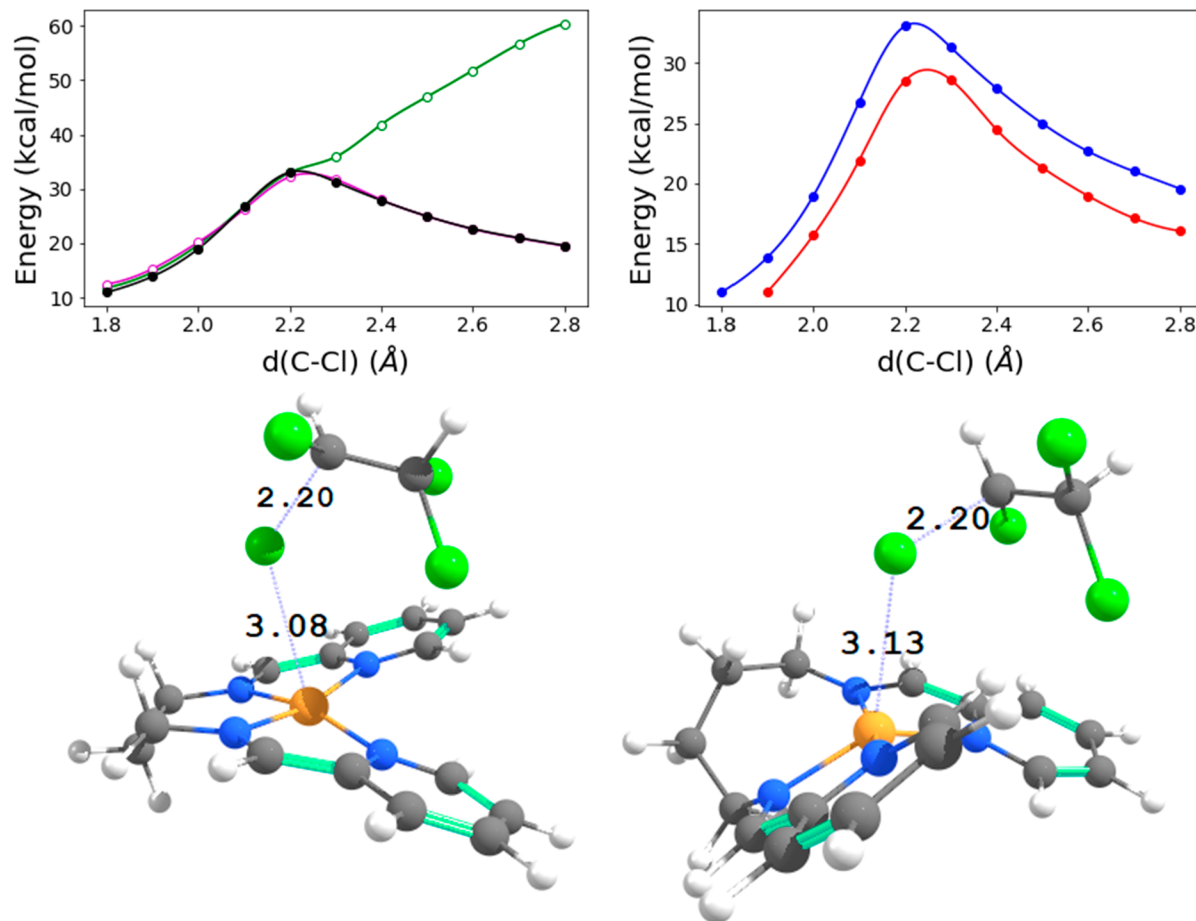


Figure 10. Top, left: energy of the closed shell singlet (green), lowest triplet (magenta), and unrestricted singlet (black) for $[\text{Cu}^1(\text{L}_3)]^+$. Top, right: open shell singlet surface for $[\text{Cu}^1(\text{L}_3)]^+$ (blue) and $[\text{Cu}^1(\text{L}_4)]^+$ (red). The zero of energy is the sum of the isolated reactants. Bottom: molecular geometries at C–Cl 2.2 Å for $[\text{Cu}^1(\text{L}_3)]^+$ (left) and $[\text{Cu}^1(\text{L}_4)]^+$ (right). Color code: Cu, orange; Cl, green; N, blue; C, gray; H, white.

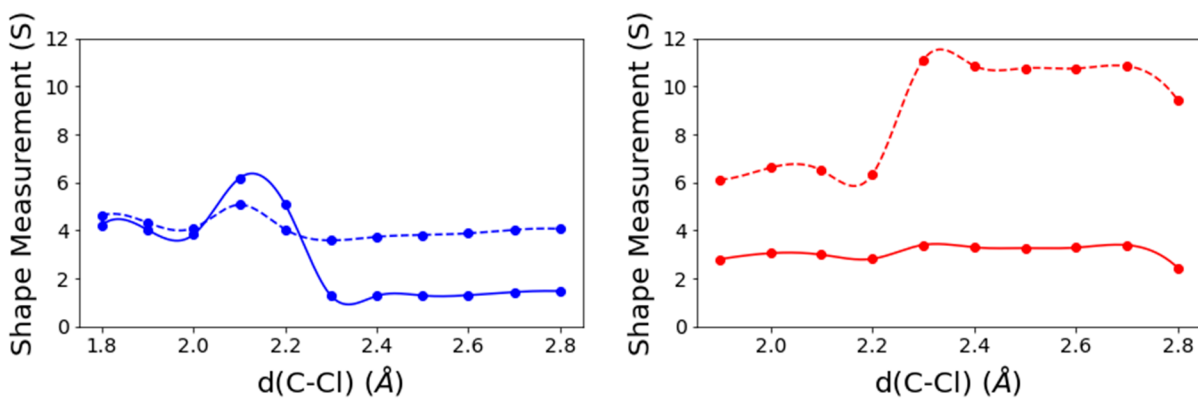


Figure 11. Continuous shape measurements for the CuN_4Cl fragment of $[\text{Cu}^1(\text{L}_3)]^+$ (blue) and $[\text{Cu}^1(\text{L}_4)]^+$ (red). Reference shapes are the trigonal bipyramidal (solid lines) and square pyramid (dashed lines). In the case of a square pyramid, the chlorine atom is forced to occupy the axial position.

are similar and around 4. It is important to note that the chlorine atom was forced to occupy the axial position in the square-pyramidal measure to have a consistent picture about the halogen attack to the planar CuN_4 fragment. The deviation increases close to the energy maximum, and the square-planar structure has the lower distortion parameter in this region. After electron/halogen transfer, the coordination environment

approaches to a trigonal bipyramidal while square-planar deviation stays in a range close to $S = 4$.

$[\text{Cu}^1(\text{L}_4)]^+$ exhibits a marked preference for the trigonal-bipyramidal conformation, with a relatively small deviation (ca. $S = 3$) that remains constant along the reaction path. In contrast, deviation with respect to square pyramid is significantly larger and further increases after electron transfer.

In summary, $[\text{Cu}^{\text{l}}(\text{L}_4)]^+$ favors a trigonal-bipyramidal coordination for the CuN_4Cl fragment along the complete reaction path, which does not require significant distortion to trigger chlorine transfer. The tension exerted by the L_4 ligand is favorable to adopt a conformation convenient for reductive dehalogenation of TCE. In contrast, $[\text{Cu}^{\text{l}}(\text{L}_3)]^+$ must experience a significant geometric distortion before chlorine transfer, penalizing reactivity. These structural differences clarify the apparent contradiction between flattening and reactivity for both compounds, since $[\text{Cu}^{\text{l}}(\text{L}_4)]^+$ does not need to be flattened to accommodate a fifth coordination in an axial position because its reaction pathway involves a trigonal-bipyramidal conformation rather than a square pyramid.

Recently, Hagen has coined the term of “ecstatic state” to illustrate how, in general words, a finite manifold of conformations representing a distribution of coordination geometries in the active site boost the activity of metalloproteins, where such a site is not considered to be entatic under usually used parameters.²⁴ Then, entatic and ecstatic must be considered as jointly operating states. Despite the author raising this concept for proteins, Hagen’s hypothesis connects with our results at the point that flexibility of coordinative environment (ligand in both cases) contributes to the achievement of unimolecular transition states of low energy with impact in the electron transfer rates.

This is valid when the geometries of the complex derived from L_3 , in both oxidized and reduced forms, can be interpreted as energized states respect to expected ideal geometries for each oxidation state, as discussed before, which does not ensure a faster electron transfer if the reaction pathway requires some degree of adaptability of the ligand. Consequently, the flexibility of the ligand to provide a pool of convenient geometries through the reaction pathway is a factor to be considered besides others such as flattening distortion, redox potentials, and the minimum structural distortion (entatic state), which are under current knowledge. In the studied case, $[\text{Cu}^{\text{l}}(\text{L}_4)]^+$ has the correct ligand flexibility to favor a smooth reaction path associated with a trigonal-bipyramidal coordination environment, as evidenced in the almost horizontal evolution of the CShM for this shape (solid red line in Figure 11). In contrast, halogen transfer to the axial position of a square pyramid requires a drastic geometry distortion as deduced from the step observed for this curve (red dashed line). Thus, planarity of the CuN_4 fragment is not a key requirement since the reaction path is not associated with a square-pyramidal coordination. Instead, ligand strain favors a vacant trigonal-bipyramidal geometry for the CuN_4 fragment, which is ideal to accept the chlorine atom in the equatorial position. In the case of $[\text{Cu}^{\text{l}}(\text{L}_3)]^+$, significant geometry distortion is observed for both reference shapes along the reaction path. L_3 is not a very flexible ligand, rising the activation energy in line with theoretical calculations and their slower oxidation kinetics.

3. CONCLUSIONS

Monometallic complexes $[\text{Cu}^{\text{l}}(\text{L}_n)]^+$ are released from dissociation of bimetallic precursors in a reversible process strongly determined by the number of methylenes in the spacers bridging coordinating moieties of the Schiff-base ligands L_n ($n = 3–7$). The systematic variation in the length of L_n has provided a range of geometries around Cu^{l} in the monomers, which follow a distortion path between square

planar when L_3 is the ligand, toward more tetrahedral complexes with Cu^{l} coordinated to L_6 and L_7 .

The gradual flattening of the complexes as the ligands become shorter is accompanied by the splitting of their MLCT bands. Theoretical results have a good match with the experimental ones, allowing us to understand the electronic behavior in terms of the bifurcation of the frontier orbitals involved in the absorption phenomena. Electrochemical studies agree with what it is expected for Cu^{l} complexes, this is oxidation of the metal is favored as the geometry is flattened. Furthermore, a linear correlation between experimental oxidation potentials and calculated shape parameters was observed in this series, which is useful to predict reactivity based on geometrical distortion of a copper complex, in a potential window of 370 mV.

After summarizing characterization results, we can indicate that the reductive dehalogenation of TCE follows a general trend where more flattened complexes have a faster ET from Cu^{l} to the halocarbon, which is also in line with the oxidation potentials measured. However, the kinetic of reaction of the most flattened and more reductant complex $[\text{Cu}^{\text{l}}(\text{L}_3)]^+$ was unexpectedly slower than the L_4 derived complex. Also, the high correspondence between both the reduced and oxidized forms of this complex seem to contravene the entatic state principle, which has been often invoked for copper coordination compounds in recent years.

Computational studies point to the impact of ligand flexibility and the prominent role of trigonal-bipyramidal coordination geometry as key factors explaining the faster oxidation kinetics of $[\text{Cu}^{\text{l}}(\text{L}_4)]^+$. In this way planarity of the CuN_4 fragment is not a requirement to get a properly energized reactant from the entatic principle perspective.

■ ASSOCIATED CONTENT

SI Supporting Information

The Supporting Information is available free of charge at <https://pubs.acs.org/doi/10.1021/acs.inorgchem.0c02037>.

Experimental procedures, crystallographic information, cyclic voltammetry, theoretical calculations and kinetic information (PDF)

Accession Codes

CCDC 1832683 and 1832684 contain the supplementary crystallographic data for this paper. These data can be obtained free of charge via www.ccdc.cam.ac.uk/data_request/cif, or by emailing data_request@ccdc.cam.ac.uk, or by contacting The Cambridge Crystallographic Data Centre, 12 Union Road, Cambridge CB2 1EZ, UK; fax: +44 1223 336033.

■ AUTHOR INFORMATION

Corresponding Authors

Daniel Aravena — Departamento de Química de los Materiales, Facultad de Química y Biología, Universidad de Santiago de Chile, Santiago, Chile; orcid.org/0000-0003-3140-4852; Email: daniel.aravena.p@usach.cl

Luis Lemus — Departamento de Química de los Materiales, Facultad de Química y Biología, Universidad de Santiago de Chile, Santiago, Chile; orcid.org/0000-0002-5499-8115; Email: luis.lemus@usach.cl

Authors

Leonel Llanos — Departamento de Química de los Materiales, Facultad de Química y Biología, Universidad de Santiago de Chile, Santiago, Chile
Cristian Vera — Departamento de Química de los Materiales, Facultad de Química y Biología, Universidad de Santiago de Chile, Santiago, Chile
Andrés Vega — Facultad de Ciencias Exactas, Departamento de Ciencias Químicas, Universidad Andrés Bello, Viña del Mar, Chile; Centro para el Desarrollo de Nanociencias y Nanotecnología, CEDENNA, Santiago, Chile; orcid.org/0000-0001-6501-4161

Complete contact information is available at:
<https://pubs.acs.org/10.1021/acs.inorgchem.0c02037>

Notes

The authors declare no competing financial interest.

ACKNOWLEDGMENTS

L.L., D.A., and C.V. thank Fondecyt for projects 1190763, 1170524, and 3170661, respectively. A.V. thanks Financiamiento Basal AFB 180001 (CEDENNA) for support. Powered@NLHPC: This research was partially supported by the supercomputing infrastructure of the NLHPC (ECM-02).

REFERENCES

- (1) Li, H.; Jiao, M.; Chen, J.; Liang, Y. Roles of zinc and copper in modulating the oxidative refolding of bovine copper, zinc superoxide dismutase. *Acta Biochim. Biophys. Sin.* **2010**, *42*, 183–194.
- (2) Lange, J.; Elias, H.; Paulus, H.; Müller, J.; Weser, U. Copper(II) and Copper(I) complexes with an open-chain N₄ Schiff base ligand modeling CuZn superoxide dismutase: Structural and spectroscopic characterization and kinetics of electron transfer. *Inorg. Chem.* **2000**, *39*, 3342–3349.
- (3) Santos, M. L. P.; Bagatin, I. A.; Pereira, E. M.; Da Costa Ferreira, A. M. Redox behaviour and reactivity of some di-Schiff base copper(II) complexes towards reduced oxygen species. *J. Chem. Soc., Dalton Trans.* **2001**, 838–844.
- (4) Linss, M.; Weser, U. The di-Schiff-base of pyridine-2-aldehyde and 1,4-diaminobutane, a flexible Cu(I)/Cu(II) chelator of significant superoxide dismutase mimetic activity. *Inorg. Chim. Acta* **1986**, *125*, 117–121.
- (5) Xi, Y.-T.; Wei, P.-J.; Wang, R.-C.; Liu, J.-G. Bio-inspired multinuclear copper complexes covalently immobilized on reduced graphene oxide as efficient electrocatalysts for the oxygen reduction reaction. *Chem. Commun.* **2015**, *51*, 7455–7458.
- (6) Zhao, Y.-M.; Yu, G.-Q.; Wang, F.-F.; Wei, P.-J.; Liu, J.-G. Bioinspired transition-metal complexes as electrocatalysts for the oxygen reduction reaction. *Chem. - Eur. J.* **2019**, *25*, 3726–3739.
- (7) Schultz, A.; Jonas, U.; Hammer, E.; Schauer, F. Dehalogenation of chlorinated hydroxybiphenyls by fungal laccase. *Appl. Environ. Microbiol.* **2001**, *67*, 4377–4381.
- (8) Szatkowski, L.; Dybala-Defratyka, A. A computational study on enzymatically driven oxidative coupling of chlorophenols: An indirect dehalogenation reaction. *Chemosphere* **2013**, *91*, 258–264.
- (9) Yang, Y.; Wei, Q.; Zhang, J.; Xi, Y.; Yuan, H.; Chen, C.; Liu, X. Degradation of MXC by host/guest-type immobilized laccase on magnetic tubular mesoporous silica. *Biochem. Eng. J.* **2015**, *97*, 111–118.
- (10) Arnold, W.; Winget, P.; Cramer, C. Reductive Dechlorination of 1,1,2,2-tetrachloroethane. *Environ. Sci. Technol.* **2002**, *36*, 3536–3541.
- (11) Lucchese, B.; Humphreys, K.; Lee, D.-H.; Incarvito, C.; Sommer, R.; Rheingold, A.; Karlin, K. Mono-, Bi-, and trinuclear Cu^{II}-Cl containing products based on the tris(2-pyridylmethyl)amine chelate derived from Copper(I) complex dechlorination reactions of chloroform. *Inorg. Chem.* **2004**, *43*, 5987–5998.
- (12) Maiti, D.; Sarjeant, A.; Itoh, S.; Karlin, K. Suggestion of an organometallic intermediate in an intramolecular dechlorination reaction involving Copper(I) and a ArCH₂Cl moiety. *J. Am. Chem. Soc.* **2008**, *130*, 5644–5645.
- (13) Rorabacher, D. Electron transfer by copper centers. *Chem. Rev.* **2004**, *104*, 651–697.
- (14) Ambundo, E.; Deydier, M.; Grall, A.; Aguera-Vega, N.; Dressel, L.; Cooper, T.; Heeg, M.; Ochrymowycz, L.; Rorabacher, D. Influence of coordination geometry upon Copper(II/I) redox potentials. Physical parameters for twelve copper tripodal ligand complexes. *Inorg. Chem.* **1999**, *38*, 4233–4242.
- (15) Yokoi, H.; Addison, A. W. Spectroscopic and redox properties of pseudotetrahedral copper(II) complexes. Their relation to copper proteins. *Inorg. Chem.* **1977**, *16*, 1341–1349.
- (16) Dennison, C. Investigating the structure and function of cupredoxins. *Coord. Chem. Rev.* **2005**, *249*, 3025–3054.
- (17) Yu, Q.; Salhi, C.; Ambundo, E.; Heeg, M.; Ochrymowycz, L.; Rorabacher, D. Direct Evidence for a geometrically constrained “entatic state” effect on Copper(II/I) electron-transfer kinetics as manifested in metastable intermediates. *J. Am. Chem. Soc.* **2001**, *123*, 5720–5729.
- (18) Comba, P. Coordination compounds in the entatic state. *Coord. Chem. Rev.* **2000**, *200*–202, 217–245.
- (19) Stanek, J.; Hoffmann, A.; Herres-Pawlis, S. Renaissance of the entatic state principle. *Coord. Chem. Rev.* **2018**, *365*, 103–121.
- (20) Comba, P.; Fath, A.; Kühner, A.; Nuber, B. Preorganization of Tetrathiamacroyclic Ligands: Implications from Computed and Experimentally Determined Structures. *J. Chem. Soc., Dalton Trans.* **1997**, *11*, 1889–1898.
- (21) Dicke, B.; Hoffmann, A.; Stanek, J.; Rappaport, M. S.; Grimm-Lebsanft, B.; Biebl, F.; Rukser, D.; Maerz, B.; Görries, D.; Naumova, M.; Biednov, M.; Neuber, G.; Wetzel, A.; Hofmann, S. M.; Roedig, P.; Meents, A.; Bielecki, J.; Andreasson, J.; Beyerlein, K. R.; Chapman, H. N.; Bressler, C.; Zinth, W.; Rüthausen, M.; Herres-Pawlis, S. Transferring the entatic-state principle to copper photochemistry. *Nat. Chem.* **2018**, *10*, 355–362.
- (22) Dahl, E.; Szymczak, N. Hydrogen bonds dictate the coordination geometry of copper: Characterization of a square-planar Copper(I) complex. *Angew. Chem., Int. Ed.* **2016**, *55*, 3101–3105.
- (23) Chaka, G.; Sonnenberg, J.; Schlegel, H.; Heeg, M.; Jaeger, G.; Nelson, T.; Ochrymowycz, L.; Rorabacher, D. A definitive example of a geometric “entatic state” effect: Electron-transfer kinetics for a Copper(II/I) complex involving a quinquedentate macrocyclic trithiaether–bipyridine ligand. *J. Am. Chem. Soc.* **2007**, *129*, 5217–5227.
- (24) Hagen, W. Hypothesis: Entatic versus ecstatic states in metalloproteins. *Metalloproteins* **2019**, *11*, 1768–1778.
- (25) Xie, B.; Elder, T.; Wilson, L.; Stanbury, D. Internal reorganization energies for copper redox couples: The slow electron-transfer reactions of the [Cu^{II/I}(bib)₂]^{2+/-} couple. *Inorg. Chem.* **1999**, *38*, 12–19.
- (26) Vallee, B.; Williams, R. Metalloenzymes: the entatic nature of their active sites. *Proc. Natl. Acad. Sci. U. S. A.* **1968**, *59*, 498–505.
- (27) Stroscio, G.; Ribson, R.; Hadt, R. Quantifying entatic states in photophysical processes: Applications to copper photosensitizers. *Inorg. Chem.* **2019**, *58*, 16800–16817.
- (28) Vallejo, J.; Pardo, E.; Viciana-Chumillas, M.; Castro, I.; Amorós, P.; Déniz, M.; Ruiz-Pérez, C.; Yuste-Vivas, C.; Krzystek, J.; Julve, M.; Lloret, F.; Cano, J. Reversible solvatomagnetic switching in a single-ion magnet from an entatic state. *Chem. Sci.* **2017**, *8*, 3694–3702.
- (29) Lemus, L.; Guerrero, J.; Costamagna, J.; Estiu, G.; Ferraudi, G.; Lappin, A. G.; Oliver, A.; Noll, B. Unfolding of the [Cu₂(1,3-bis(9-methyl-1,10-phenanthrolin-2-yl)propane)]²⁺ helicate. Coupling of the chlorocarbon dehalogenation to the unfolding process. *Inorg. Chem.* **2010**, *49*, 4023–4035.

- (30) Lemus, L.; Guerrero, J.; Costamagna, J.; Lorca, R.; Jara, D.; Ferraudi, G.; Oliver, A.; Lappin, A. G. Resolution and characterization of helicate dimer and trimer complexes of 1,3-bis(9-methyl-1,10-phenanthrolin-2-yl)propane with Copper(I). *Dalton Trans.* **2013**, *42*, 11426–11435.
- (31) Díaz, D.; Llanos, L.; Arce, P.; Lorca, R.; Guerrero, J.; Costamagna, J.; Aravena, D.; Ferraudi, G.; Oliver, A.; Lappin, A. G.; Lemus, L. Steric and electronic factors affecting the conformation of bimetallic Cu(I) complexes: Effect of the aliphatic spacer of tetracoordinating Schiff-base ligands. *Chem. - Eur. J.* **2018**, *24*, 13839–13849.
- (32) Tao, J.; Perdew, J. P.; Staroverov, V. N.; Scuseria, G. E. Climbing the density functional ladder: Nonempirical meta-generalized gradient approximation designed for molecules and solids. *Phys. Rev. Lett.* **2003**, *91*, 146401.
- (33) Schäfer, A.; Huber, C.; Ahlrichs, R. Fully optimized contracted Gaussian basis sets of triple zeta valence quality for atoms Li to Kr. *J. Chem. Phys.* **1994**, *100*, 5829–5835.
- (34) Weigend, F.; Ahlrichs, R. Balanced basis sets of split valence, triple zeta valence and quadruple zeta valence quality for H to Rn: Design and assessment of accuracy. *Phys. Chem. Chem. Phys.* **2005**, *7*, 3297–3305.
- (35) Mennucci, B.; Tomasi, J. Continuum solvation models: A new approach to the problem of solute's charge distribution and cavity boundaries. *J. Chem. Phys.* **1997**, *106*, 5151–5158.
- (36) Yang, L.; Powell, D. R.; Houser, R. P. Structural variation in copper(I) complexes with pyridylmethylamide ligands: structural analysis with a new four-coordinate geometry index, τ_4 . *Dalton Trans.* **2007**, 955–964.
- (37) Okuniewski, A.; Rosiak, D.; Chojnacki, J.; Becker, B. Coordination polymers and molecular structures among complexes of mercury(II) halides with selected 1-benzoylthioureas. *Polyhedron* **2015**, *90*, 47–57.
- (38) Sánchez-Lombardo, I.; Alvarez, S.; McLauchlan, C. C.; Crans, D. C. Evaluating Transition State Structures of Vanadium-Phosphatase Protein Complexes Using Shape Analysis. *J. Inorg. Biochem.* **2015**, *147*, 153–164.
- (39) Alvarez, S.; Alemany, P.; Casanova, D.; Cirera, J.; Llunell, M.; Avnir, D. Shape maps and polyhedral interconversion paths in transition metal chemistry. *Coord. Chem. Rev.* **2005**, *249*, 1693–1708.
- (40) Casanova, D.; Cirera, J.; Llunell, M.; Alemany, P.; Avnir, D.; Alvarez, S. Minimal distortion pathways in polyhedral rearrangements. *J. Am. Chem. Soc.* **2004**, *126*, 1755–1763.
- (41) Llunell, M.; Casanova, D.; Cirera, J.; Alemany, P.; Alvarez, S. Shape 2.0, Program for the Stereochemical Analysis of Molecular Fragments by Means of Continuous Shape Measures and Associated Tools, 2010.
- (42) Miller, M.; Gantzel, P.; Karpishin, T. Effects of sterics and electronic delocalization on the photophysical, structural, and electrochemical properties of 2,9-disubstituted 1,10-phenanthroline copper(I) complexes. *Inorg. Chem.* **1999**, *38*, 3414–3422.
- (43) Phifer, C.; McMillin, D. The basis of aryl substituent effects on charge-transfer absorption intensities. *Inorg. Chem.* **1986**, *25*, 1329–1333.
- (44) Zerk, T.; Bernhardt, P. Redox-coupled structural changes in copper chemistry: Implications for atom transfer catalysis. *Coord. Chem. Rev.* **2018**, *375*, 173–190.
- (45) Isse, A.; Gennaro, A.; Lin, C.; Hodgson, J.; Coote, M.; Guliashvili, T. Mechanism of carbon–halogen bond reductive cleavage in activated alkyl halide initiators relevant to living radical polymerization: Theoretical and experimental study. *J. Am. Chem. Soc.* **2011**, *133*, 6254–6264.
- (46) Addison, A. W.; Rao, N. T.; Reedijk, J.; van Rijn, J.; Verschoor, G. C. Synthesis, structure, and spectroscopic properties of copper(II) compounds containing nitrogen–sulphur donor ligands; the crystal and molecular structure of aqua[1,7-bis(*N*-methylbenzimidazol-2'-yl)-2,6-dithiaheptane]copper(II) perchlorate. *J. Chem. Soc., Dalton Trans.* **1984**, 1349–1356.
- (47) Bhattacharyya, A.; Bhaumik, P. K.; Bauzá, A.; Jana, P. P.; Frontera, A.; Drew, M. G. B.; Chattopadhyay, S. A Combined Experimental and Computational Study of Supramolecular Assemblies in Ternary Copper(II) Complexes with a Tetradentate N4 Donor Schiff Base and Halides. *RSC Adv.* **2014**, *4*, 58643–58651.
- (48) Xie, B.; Wilson, L.; Stanbury, D. Cross-electron-transfer reactions of the $[\text{Cu}^{\text{II}/\text{I}}(\text{bite})]^{2+/+}$ redox couple. *Inorg. Chem.* **2001**, *40*, 3606–3614.
- (49) Fang, C.; Fantin, M.; Pan, X.; de Fiebre, K.; Coote, M. L.; Matyjaszewski, K.; Liu, P. Mechanistically Guided Predictive Models for Ligand and Initiator Effects in Copper-Catalyzed Atom Transfer Radical Polymerization (Cu-ATRP). *J. Am. Chem. Soc.* **2019**, *141*, 7486–7497.
- (50) Chai, J. DA.; Head-Gordon, M. Long-Range Corrected Hybrid Density Functionals with Damped Atom-Atom Dispersion Corrections. *Phys. Chem. Chem. Phys.* **2008**, *10*, 6615–6620.